A FINITE ELEMENT MODEL FOR THE SIMULATION OF DIRECT METAL DEPOSITION
Paper #1801

Guillaume Marion[1], Georges Cailletaud[1], Christophe Colin[1], Matthieu Mazière[1]

[1]Mines ParisTech, PSL Research University
Centre des matériaux, CNRS UMR 7633, BP 87, 91003 Evry, France

Abstract

The life prediction of components built by additive manufacturing process, such as Direct Metal Deposition (DMD), needs a good characterization of their physical states (including metallurgy, residual stresses…). A robust finite element analysis of the DMD process at a macroscopic scale should then include thermal, metallurgical and mechanical aspects. The present paper shows a comprehensive model, where the metallurgical section is developed in strong connection with the physical process. The model is implemented in the Finite Element Code Z-Set and a specific strategy is introduced to progressively activate the elements and follow a given fabrication route.

Introduction

Additive manufacturing is a family of processes allowing to build a part from a CAD file by adding material where it is needed, layer after layer. Various materials can be used with these processes such as polymers, ceramics or metals. This study will focus on metallic components carried out by Direct Metal Deposition (DMD), a process which consists in throwing a powder jet into a melted pool created by a laser beam, coaxial to the powder jet. Once solidified, the deposited material forms a track. The part is built by deposing the tracks the one next or over to the other (Figure 1). This process is more and more used by the aeronautical industry as it allows to build really complex shapes. It can offer great opportunity of weight saving by optimizing the design of the part and using structured materials (like 3D lattices or 3D honeycomb). The process is also convenient to design a single component instead of a set of assembled parts, which may also simplify the production process. Another new opportunity given by these processes is the ability to change the geometry of the part at any time without manufacturing any new tool. The aeronautical industry is also aware of improving the buy-to-fly ratio which represents the quantity or bought material that is really used to manufacture the part. With conventional machining, the buy-to-fly ratio stays around 30%, meanwhile it reaches 80%

with additive manufacturing. The life prediction of components built with this process implies to know properly their physical states (including metallurgy, residual stresses...). Some models that can be found in the literature focus on the laser/material interaction and the physical phenomena that occurs locally on the melt pool, such as fluid flow or Marangoni movements [1,2]. This type of study is useful, since it defines local boundary conditions, but their CPU time is too big to allow performing the relevant structural calculations for the estimation of residual stress fields in industrial parts.
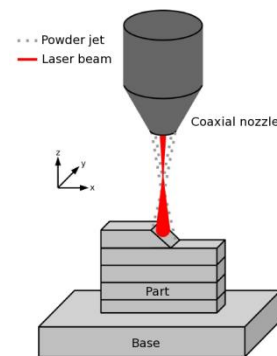

Figure 1: Direct Metal Deposition process [3,4].

A robust finite element analysis of this process at a macroscopic scale should then include thermal, metallurgical and mechanical aspects using some relevant assumptions to reduce the computation time. The present paper shows a comprehensive model, where the metallurgical section is developed in strong connection with the physical process.

The material: Ti-6Al-4V

The material used of the study is a well-known titanium alloy called Ti-6Al-4V (TA6V). This is a Ti-base alloy, with around 6wt. % of aluminum, 4wt.% of vanadium. Even if this material can be found into different phases, only three will be considered in this study as they are the most present during the process [5]. The phase α, which is at the equilibrium for low temperature is hexagonal closed packed (HCP). The

phase β has a centered cubic lattice and it is stable at high temperature. The martensitic phase α' has a hexagonal crystal structure.

Modelling strategy

In order to reduce the computation time, while preserving the most important physical phenomena, only the relevant interactions are introduced in the model (Figure 2). The effect of temperature on phase change (1) and the influences of temperature (5) and phase volume fractions (3) on the mechanical behaviors are taken into account. Both latent heat of fusion (2) and plasticity induced thermal dissipation (6) are ignored due to their low contributions to the thermal evolutions if compared with the effect of the laser beam. The stress induced phase transformations (4) are also ignored compared to the phase transformations coming from the thermal cycles.
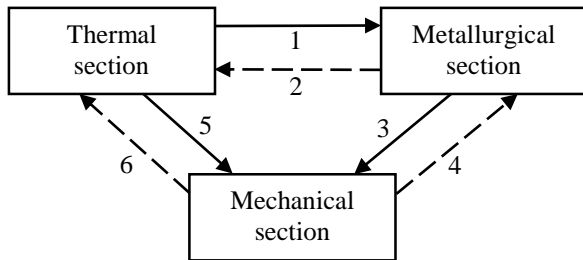

Figure 2 : The three sections of the model and their interactions [4].

The three sections of the model (thermal, metallurgical and mechanical) are then run sequentially. The model is implemented in the Finite Element Code Z-set (http://www.zset-software.com/).

The fluid flow is not taken into account. Due to this assumption, the model cannot predict the geometry of the tracks. In fact, all the elements are parallelepipedic, so that the track section is simply rectangular. The size (thickness, width...) must be known before the computation. It depends on the process parameters such as the laser power, the scanning velocity or the powder feed rate. These values can be obtained from experiments or using a local model which takes into account fluid flow.

A specific strategy is introduced to simulate the deposition of material according to a given fabrication route. At the first iteration, all the elements corresponding to the part are "empty". Young's modulus and thermal conductivity are set to 0. As shown in Figure 3, an activation zone follows the laser spot. If an element belongs to this area, its thermal and

mechanical properties are automatically set to the correct values, so that it becomes "active".
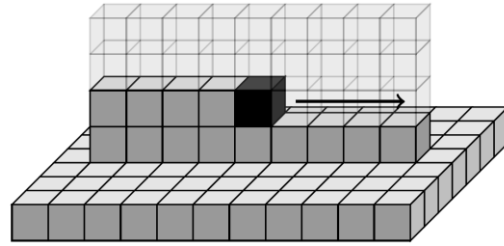

Figure 3: Elements activation.

Once an element is activated, the external surface of the active element set is updated in order to apply the correct boundary conditions. It is thus possible to study the effects of using different laser paths on the evolution of stress and strain fields. For example, during the manufacturing of a multi-layered part, the deposition of one layer can be done by deposing successive tracks in lines, in concentric circles or one continuous track in spiral, etc… (Figure 4). This will directly affect the thermal history of the part and thus, the generation of stress and strain fields.
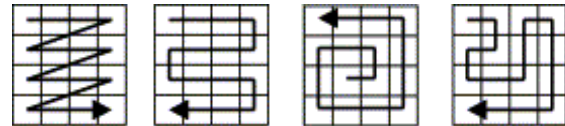

Figure 4: Exemple of laser paths.

As the thermal phenomena are at the origin of all the mechanical loadings and microstructural modifications of the part during the process, the results of the thermal model are critical. An experimental investigation was done to characterize the temperature evolutions and the thermal gradients during the building of a wall.

Characterization of the thermal loadings

During the building of a wall, the laser beam will pass several times through one given point of the part. This leads to intense thermal cycling and to the formation of thermal gradients, as shown by Maisonneuve [5], who performed several experimental runs to quantify theses phenomena. One of the experiments consisted in measuring the temperature in one given point with a laser pyrometer during the building of a wall, (Figure 5).

Figure 6 shows the temperature evolution measured in the middle of the sixth deposited track. The first five temperature peaks are not relevant since they

correspond to a temperature measurement of the powder particles or gas environment as the wall was not built yet at this place.
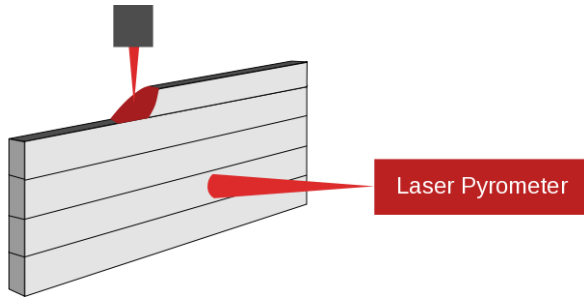

Figure 5 : Experimental method of the temperature measurement in a given point of a wall during its building.

The sixth peak represents the first measurement in a deposited layer. This plot shows that temperature peaks observed during the deposition of the successive layers can be higher than the melting point. It is the remelting zone. After these first peaks, the maximum temperature decreases up to the last cycles that can be considered as an annealing phase. Since the spot of the laser pyrometer was bigger than the melt pool, the measured temperatures are underestimated.
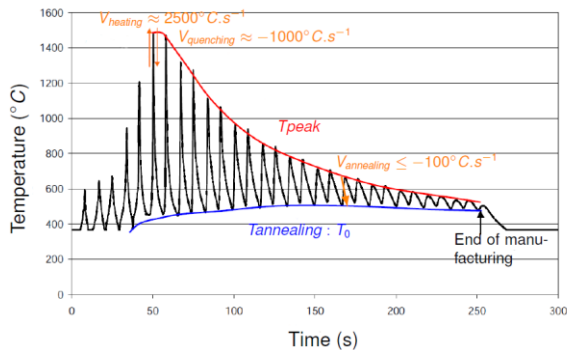

Figure 6: Thermal evolution on a point located on the bottom of a wall during its build [5].

The previous experiment has been done several times to observe the thermal gradient all along the wall during the building. For each new experiment, the laser pyrometer position was changed. The thermal evolution can then be plotted as a function of time at different points of the wall, so that the thermal gradient along the part can also be characterized. This gradient is shown in Figure 7. The maximum value of temperature can be found in the melt pool. Then, the temperature decreases with the distance from the melt pool. It demonstrates that there is a competition between the heat sources, the laser, and the heat

dissipations, which occurs essentially in the substrate of the build.

Residual stress fields are produced by these important thermal evolutions and gradients. This is the reason why the substrate is often heated before manufacturing. Indeed, if the substrate temperature increases, the gradient between the melt pool and the substrate is less important and there are less residual stresses in the part.
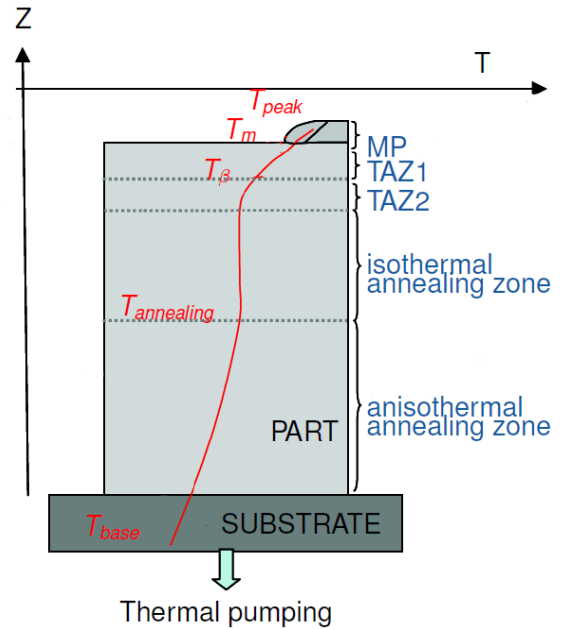

Figure 7 : Thermal gradients in a wall during its build [3,4].

Thermal model

A model has been introduced in a past study [3,4], based on an equilibrium equation between the surface thermal flux representing the effect of the laser and the leaks due to conduction, radiation and convection. This model cannot be compared to the previously shown measurements since they are known to be underestimated. A new experiment has been done, in which the temperature has been measured at three points of the substrate using thermocouples. A good agreement is obtained between these measurements and the results of the model. More details about this model and its validation can be found in the original document [3,4].

After its validation on a global scale, the model helps understanding the thermal history at a local scale. Figure 8 shows the thermal evolution of the point corresponding to Maisonneuve's measurements [5].

The model provides also the temperature rates at any point of the component. Figure 9 shows a plot of the temperature versus the temperature rate during a test. The temperature rates are higher during heating than during cooling and the value of the temperature rate decreases when the temperature decreases. At the end of the process, the temperature rate tends to zero and the peak temperature tends towards a steady state which corresponds to the annealing temperature.
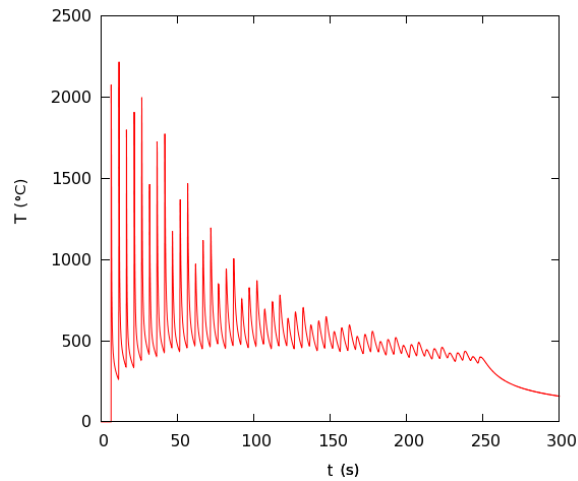

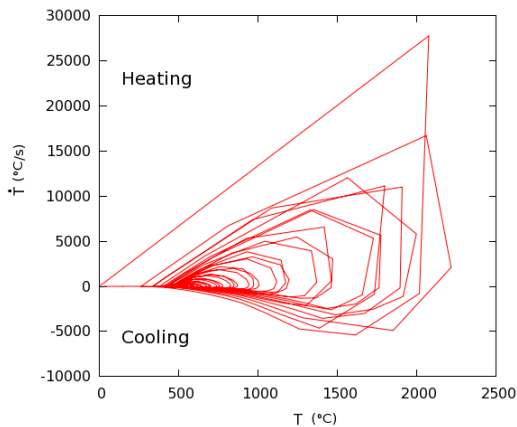Figure 8 : Temperature history for a point located at the bottom of the wall.

Figure 9 : Temperature versus temperature rate.

Finally, an interesting result of this model is the spatial evolution of the temperature during the process (Figure 10).

The building program is simulated by means of a numerical process that allows to define complex tracks in 3D components, to dynamically activate elements and to update boundary conditions. The example shown in Figure 11 is a cube built by deposition of five layers, each of them being made of six consecutive tracks. The track orientations are rotated by 90° between each layer.
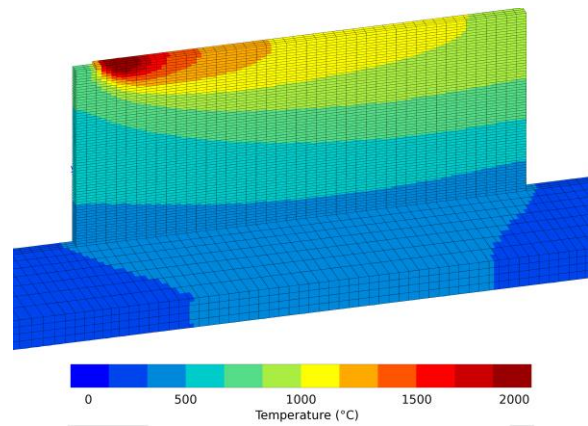

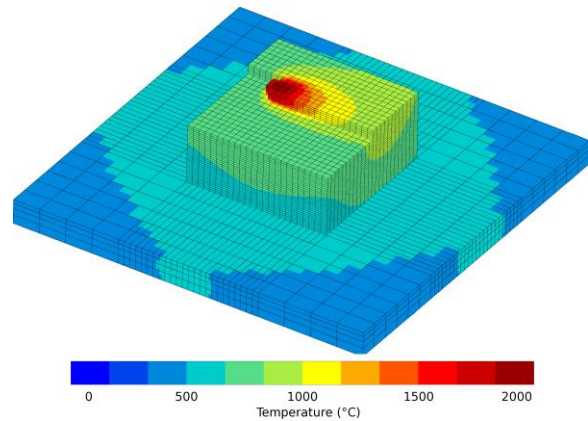Figure 10: Temperature field during the build of a wall.

Figure 11: Temperature field during the build of a cube shaped specimen.

Metallurgy

Phase transformation

After the solidification, the last melt pool and Temperature Affected Zone 1 (TAZ 1) are fully composed of β phase (Figure 7). The evolution of the phase fractions during cooling will then depend on the cooling rate. All the possible transformations are presented in Figure 12 and will be described below.

A low cooling rate (under 410°C/s) will initiate the diffusion transformation of β into α phase. The fraction of α phase in the alloy is determined by the β→α law kinetics, which is usually represented by a continuous cooling transformation diagram, [6].

For cooling rate larger than 410°C/s, β phase transforms by a martensitic mechanism without

diffusion into the non-equilibrium α' phase. The martensite start temperature (Ms) of Ti-6Al-4V has been determined experimentally towards 650°C by Castro et al [9] and Elmer et al [7]. The results of Elmer et al [7] show that the martensite finish temperature is 400°C.
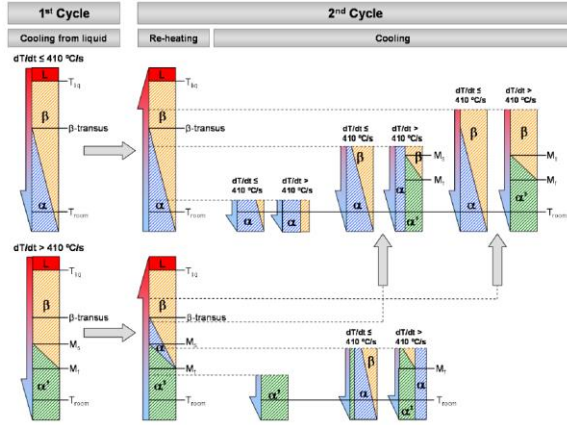

Figure 12: Phase evolutions induced by the different thermal loadings [6].

If the cooling starts from a α+β domain, the transformations are slightly different. For temperature rates above 410°C/s where vanadium diffusion is difficult, a part of β is retained after cooling at low temperature depending on the proportion of this β phase present in the alloy at high temperature. In equilibrium, the concentration of vanadium in the β phase increases while decreasing volume fraction of this phase at high temperature. For a volume fraction of β that exceeds 0.25, only a portion of β stable (rich in vanadium) will be retained at room temperature.

During heating, the α phase will be transformed into a β phase and the martensite α' into α+ β with a diffusion mechanism.

Some of the walls built by Maisonneuve [5] were stopped and analyzed before the end of the process. The various evolution types can be confirmed by interrupted tests [5]. A typical result is given in Figure 13.

Different microstructural zones can be observed. The first one corresponds to the melt pool, then there are two Temperature Affected Zones (TAZ), the first (TAZ 1) corresponds to temperatures between the transus β and the melting point and the second one (TAZ 2) between about Mf and the transus β. After cooling the first TAZ is fully β, the second one hold the α'→α+β transformation. Finally, the rest of the wall is α'+α+β because the temperature is too low to allow the complete α' destabilization. The bottom of

the wall is fully α' due to the large thermal dissipation induced by the substrate.
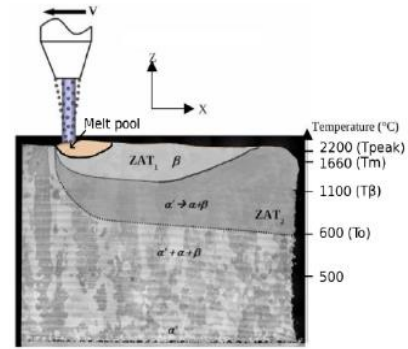

Figure 13 : Spatial distribution of the different phases during the build of a wall [5].

Metallurgical Model

The metallurgical model must be able to account the cases depending on all the thermal history mentioned in the previous sections, according to the initial state of the material and the subsequent temperature history.

Crespo [6] induced classical laws for each transformation. The main variables of the model are the volume fraction of the phases α, α' and β respectively noted z_α, $z_{\alpha'}$ and z_β. The sum of the volume fractions of all the phases must be equal to one which gives a first conservation rule (1)

$$z_\alpha + z_{\alpha'} + z_\beta = 1 \qquad (1)$$

In the following, only the volume fractions of β and α' will be computed by the model, meanwhile α phase volume fraction will be deduced using (1).

The diffusion transformations (β→α, α→β and α'→α+β) are described by a Johnson-Mehl-Avrami (JMA) equation. For a fixed temperature T:

$$z_i = (1 - \exp(-kt^n))z_{i_{eq}} \qquad (2)$$

Where $z_{i_{eq}}$ is the equilibrium proportion of phase i that can be formed at temperature T. The values of $z_{\alpha_{eq}}$ and $z_{\beta_{eq}}$ at each temperature were calculated by Castro et Seraphin [9] who found the dependence of the equilibrium volume fractions of α and β to be given by equations (6) and (7). In presence of martensite α' in the material, the equilibrium volume fraction of α and β depend on $z_{\alpha'}$ according to :

$$z_{\alpha_{eq}}(T) = z_{\alpha_{eq_0}}(T) * (1 - z_{\alpha'}) \quad (3)$$

$$z_{\beta_{eq}}(T) = z_{\beta_{eq_0}}(T) * (1 - z_{\alpha'}) \quad (4)$$

The transformation of α' into α+β is slightly different because this transformation is non reversible. During heating, the maximum amount of α' that can be transformed at each temperature is given by Mur et al [10]. It is approximated by :

$$z_{\alpha'_{eq}} = \frac{1}{2}\left(1 + \tanh\left(\frac{450-T}{80}\right)\right) \quad (5)$$

The comparison of the experimental values of $z_{\alpha'_{eq}}$ given by Mur et al [10] and this expression is shown in the Figure 14.
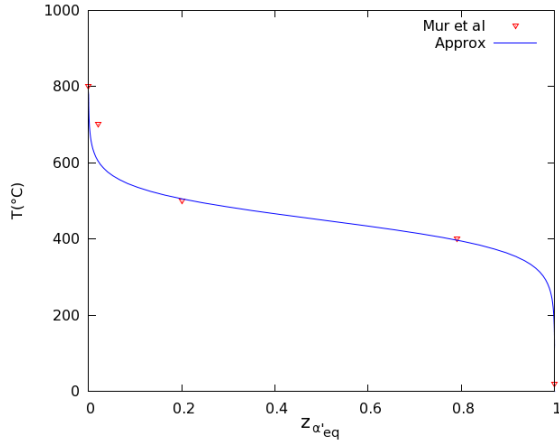

Figure 14: Equilibrium volume fraction of α' to be transformed versus temperature, as cooling.

The transformation can only happen when $z_{\alpha'} > z_{\alpha'_{eq}}$, so that the amount of transformed α' phase is replaced by the sum of the equilibrium volume fraction of α and β at the given temperature.

The values of the coefficients k and n are given by Malinov et al [6] for the transformations β→α and α→β (Table 1), and by Mur et al [10] for the transformation α'→α+β (Table 2). The values that were not found in the literature were fitted, respecting some constraints. Under 400°C/s, the value of k tend to zero in order to have a very slow kinetics. On the contrary, the values of k must be largest above

1200°C, in order to transform all the present phases into β.

The classical shape of JMA's equations is given for isothermal transformations. A rate form of the equations has to be used in the case of anisothermal transformations. These expressions are then integrated with a Runge-Kutta algorithm. For any type of temperature history.

Table 1: JMA parameters for α↔β transformations

T	n_1	k_1
750	1.40	0.028
800	1.34	0.026
850	1.38	0.022
870	1.34	0.025
900	1.21	0.046
920	1.39	0.024
950	1.41	0.017

Table 2: JMA parameters for α'→α+β transformation

T	n_2	k_2
400	0.667	0.0192
500	1.106	0.0147
700	1.252	0.0246
800	1.326	0.0307

For the transformations by diffusion involving α and β, the evolution rules are expressed as in the equation (11).

$$z_{\alpha_{eq_0}}(T) = \begin{cases} 0.925(1 - e^{0.0085(980-T)}), & T \leq T_{\beta_{eq}} (980°C) \\ 0, & T > T_{\beta_{eq}} (980°C) \end{cases} \quad (6)$$

$$z_{\beta_{eq_0}} = 1 - z_{\alpha_{eq}} \quad (7)$$

For the particular case where α' is transformed into α+β during heating, only the case where $z_{\alpha'} > z_{\alpha'_{eq}}$ can be considered and the amount of α' transformed into β during the transformation must be added to the evolution equation of β which gives the expressions (12) and (13).

Martensitic transformation

The amount of martensite formed depends essentially on the undercooling below the martensite start temperature (Ms) and is given in simple conditions by the Koistinen-Marburger equation.

$$z_{\alpha'} = 1 - \exp(-\gamma(M_s - T)) \qquad (8)$$

where γ is a constant. The values of M_s, M_f and γ were calculated on the basis of results obtained by Elmer et al [7].

The previous expression has to be updated to take into account the eventual amount of α' already present at the beginning of the transformation and the retained β, in the new expression (14), where $z_\beta(T_0)$ is the volume fraction of β phase at the temperature of the beginning of the transformation T_0 and z_{β_r} the volume fraction of retained β. z_{β_r} is expressed in order to retain all the

β phase if $z_\beta(T_0)$ is under 0.25 and to retain only a certain amount of β if $z_\beta(T_0)$ is above 0.25. The expression of z_{β_r} is given by equation (15). The expression of $z_{\alpha'}$ is then given by equation (16).

The exponential part can be eliminated thanks to expression (14), so that :

$$-\exp(-\gamma(M_s - T)) = 1 - \frac{z_{\alpha'} - z_{\alpha'}(T_0)}{z_\beta(T_0) - z_{\beta_r}} \qquad (9)$$

$$\dot{z}_{\alpha'} = \gamma\dot{T}(z_\beta(T_0) - z_{\beta_r} - z_{\alpha'} + z_{\alpha'}(T_0)) \qquad (10)$$

$$\text{If } z_\beta > z_{\beta_{eq}} : \quad \dot{z}_\beta = kn\left(z_{\beta_{eq}}(\mathrm{T}) - z_\beta\right)\left[-\frac{1}{k}\ln\left(\frac{z_\beta - z_{\beta_{eq}}(T)}{1 - z_{\beta_{eq}}(T)}\right)\right]^{\frac{n-1}{n}}$$

$$\text{If } z_\beta < z_{\beta_{eq}} : \quad \dot{z}_\beta = kn\left(z_{\beta_{eq}}(\mathrm{T}) - z_\beta\right)\left[-\frac{1}{k}\ln\left(\frac{z_{\beta_{eq}}(T) - z_\beta}{z_{\beta_{eq}}(T)}\right)\right]^{\frac{n-1}{n}} \qquad (11)$$

$$\text{If } z_\beta = z_{\beta_{eq}} \quad \text{then} \quad \dot{z}_\beta = 0.$$

$$\text{If } z_{\alpha'} < z_{\alpha'_{eq}}(T) : \quad \dot{z}_{\alpha'} = k_2 n_2\left(z_{\alpha'_{eq}}(T) - z_{\alpha'}\right)\left[-\frac{1}{k_2}\ln\left(\frac{z_{\alpha'_{eq}}(T) - z_{\alpha'}}{z_{\alpha'_{eq}}(T)}\right)\right]^{\frac{n_2-1}{n_2}} \qquad (12)$$

$$\text{If } z_\beta < z_{\beta_{eq}}(T) : \dot{z}_\beta = -\dot{z}_{\alpha'} z_{\beta_{eq}}(T) + k_1 n_1\left(z_{\beta_{eq}}(T) - z_\beta\right)\left[-\frac{1}{k_1}\ln\left(\frac{z_{\beta_{eq}}(T) - z_\beta}{z_{\beta_{eq}}(T)}\right)\right]^{\frac{n_1-1}{n_1}} \qquad (13)$$

$$z_{\alpha'} = z_{\alpha'}(T_0) + \left(z_\beta(T_0) - z_{\beta_r}\right)[1 - \exp(-\gamma(M_s - T)) \qquad (14)$$

$$z_{\beta_r} = \begin{cases} z_\beta(T_0), & z_\beta(T_0) < 0.25 \\ 0.025\,(1 - z_\beta(T_0)), & z_\beta(T_0) \geq 0.25 \end{cases} \qquad (15)$$

$$\dot{z}_{\alpha'} = \left(z_\beta(T_0) - z_{\beta_r}\right)[-\gamma\dot{T}\,\exp(-\gamma(M_s - T))] \qquad (16)$$

Comparison with experimental data

The results given by the model (Figure 15) will be compared to the phase evolutions observed by Maisonneuve [5] with four sets of process parameters.
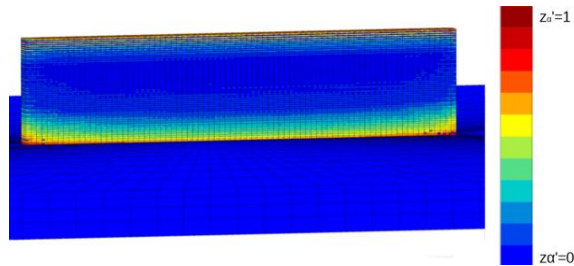

Figure 15 : Volume fraction of α' in a wall at the end of its manufacturing

Conclusion and perspectives

A global model able to estimate the residual stresses and displacements induced in a component built by the direct metal deposition process has been proposed. The model structure allows to study industrial parts in a reasonable CPU time, while including thermal, metallurgical and soon, mechanical aspects of the process. Once the model will be validated with experimental data, it will be used to optimize the process parameters. The same framework can also be used to model the selective laser melting process, another additive process in which the powder is deposited as successive layers which are selectively melted by the laser beam.

References

[1] Kong, F. & Kovacevic, R. (2010) Modeling of heat transfer and fluid flow in the laser multilayered cladding process, Metallurgical and materials transactions B, 41:1310-1320

[2] Ibarra-Medina, J., Vogel, M. & Pinkerton, A.J. (2010) A CFD model of laser cladding: from deposition head to melt pool dynamics, Physics Procedia, vol 5, 337-346

[3] Longuet, A. (2010) Modélisation du procédé de projection laser – Application au Ti-6Al-4V, PhD thesis, MINES ParisTech

[4] Longuet, A., Robert, Y., Aeby-Gautier, E., Appolaire, B., Marriage, J.F., Colin, C. & Cailletaud, G. (2009) A multiphase mechanical model for Ti-6Al-4V: Application to the modeling of laser assisted processing, Computational Materials Science, 761-766

[5] Maisonneuve, J. (2008) Fabrication directe de pièces aéronautiques en TA6V et IN718 : Projection et fusion sélective par laser, PhD thesis, MINES ParisTech

[6] Malinov, S., Markovsky, P., Sha, S. & Guo, Z. (2001) Resistivity study and computer modelling of the isothermal transformation kinetics of Ti-6Al-4V and Ti-6Al-2Sn-4Zr-2Mo-0.08Si alloys, Journal of alloys and Compounds, 314:181-192

[7] Elmer, J.W., Palmer, T.A., Babu, S.S., Zhang, W., & DebRoy, T. (2004) Phase transformations dynamics during welding of Ti-6Al-4V, Journal of Applied Physics, 95:8327-8339

[8] Crespo, A.S.S. (2010) Mathematical Simulation of Laser Powder Deposition Applied to the Production of Prostheses and Implants of Ti and Ti-6Al-4V, PhD thesis, Universidade Técnica de Lisboa

[9] Seraphin, L., Castro, R., (1966) Contribution to metallographic and structural study of titanium alloy TA6V, Memoires Scientifiques de la Revue De Metallurgie, 63:1025-1058

[10] Mur, F.X.G, Rodriguez, D. & Planell, J.A. (1996) Influence of tempering temperature and time on the alpha'-Ti-6Al-4V martensite. 234:287-289

Acknowledgements